

# The Bulk Motion of Gas in the Core of the Centaurus Galaxy Cluster

The XRISM collaboration<sup>1</sup>

<sup>1</sup>The list can be found on the last page.

## Abstract

Galaxy clusters, the largest gravitationally bound structures in the Universe, contain vast amounts of dark matter, galaxies, and hot ionised gas known as the intracluster medium (ICM). In relaxed cluster cores, the ICM appears to cool radiatively faster than the age of the cluster, but the absence of line emission from the predicted cooling rate suggests heating mechanisms that offset the cooling, with feedback from active galactic nuclei (AGNs) being the most likely source [1, 2]. Turbulence and bulk motions, such as the oscillating (“sloshing”) motion of the core gas in the cluster potential well, have also been proposed as mechanisms for the distribution of heat from the outside of the core [3, 4]. Here we present high-resolution X-ray spectroscopic observations of the core of the Centaurus galaxy cluster with the XRISM satellite. We find that the hot gas is streaming along the line of sight relative to the central galaxy (NGC 4696), with relative velocities varying from **130 km s<sup>-1</sup>** to **310 km s<sup>-1</sup>** within  $\sim$  **30 kpc** of the centre, indicating a structured bulk flow (“wind”) blowing in the core. This wind is consistent with the core gas sloshing. While the wind may prevent excessive accumulation of cooled gas at the centre of the cluster, it could also distribute the heat injected by the central AGN and/or bring in thermal energy from the surrounding ICM, thus contributing to the thermal balance at the cluster centre. The velocity dispersion (turbulent velocity) of the gas is found to be only  $\lesssim$  **120 km s<sup>-1</sup>** (corresponding to a Mach number  $\mathcal{M} \lesssim$  **0.2**) in the core, even within  $\sim$  **10 kpc** of the AGN. This may indicate that the influence of the AGN on the motion of the surrounding ICM is limited in the Centaurus cluster.

As one of the closest cool-core clusters, the Centaurus cluster is an ideal target for studying the complex physics of the ICM. Its central galaxy, NGC 4696 at a distance of 36.8 Mpc [5], hosts an AGN that has inflated numerous cavities in the surrounding X-ray gas [6] (Extended Data Fig. 2). Previous X-ray observations have revealed a

wealth of structure in the ICM, including filaments and cold fronts [6]. These features are thought to be related to AGN feedback and the sloshing of the core gas. However, the limited spectral resolution of the previous generation of X-ray observatories could not provide hard evidence to support these ideas, especially in terms of dynamics. We present new observations of the Centaurus cluster core with the X-Ray Imaging and Spectroscopy Mission (XRISM) launched in 2023 [7]. The high spectral resolution, non-dispersive Resolve microcalorimeter on XRISM provides an unprecedented view of the thermodynamics and kinematics of the ICM, allowing the first accurate measurements of the large- and small-scale gas velocities in Centaurus. The angular resolution of Resolve ( $\sim 14$  kpc for half the diameter at the distance of Centaurus) allows useful spatially resolved spectroscopy. To unravel the environment around the central AGN, we focus on the central  $r \lesssim 30$  kpc region and study the temperature structure, the bulk motions of the gas, and the turbulent velocity. Since the power of the AGN, estimated from radio luminosity and cavity size, is smaller than typical for central AGNs in other clusters [8], we expect the core of the Centaurus cluster to be less affected by AGN activity.

XRISM observed the Centaurus cluster during its performance verification phase from December 2023 to January 2024, with a total exposure time of 284.7 ksec. The aiming point for the Centaurus cluster was located at  $\sim 1'$  northwest of the central galaxy, NGC 4696, as shown in Fig. 1. The Resolve spectrum for the field of view (FOV) is shown in Fig. 2. We examine Resolve spectra in the 1.8–12 keV band for the 5 regions shown in Fig. 1. Since the point spread function (PSF) of XRISM is relatively large ( $\sim 1.3'$  for the Half Power Diameter: HPD), a significant number of photons emitted from outside a given region may be seen by the telescope as "inside" the region, and vice versa. We have accounted for this effect (referred to as spatial-spectral mixing; SSM) by fitting the spectra of the 5 regions simultaneously with plasma models and appropriate weights (Methods). We found that the spectra in each of the regions can be described by a single thermal plasma model, except for the central region ( $r \lesssim 8$  kpc from the central AGN), where two temperature components ( $T = 2.81$  and  $1.41$  keV) are required (Extended Data Table 1). For the outer regions, the temperatures are  $T \sim 2.4$ – $3.1$  keV.

Using stellar absorption data from the Multi-Unit Spectroscopic Explorer (MUSE) at the Very Large Telescope (VLT), we determine that the heliocentric velocity and redshift of the stellar system of NGC 4696 are  $V_{\text{N4696}} = 3008 \pm 7 \text{ km s}^{-1}$  and  $z_{\text{N4696}} = 0.01003$ , respectively (Methods). We find that the heliocentric redshifts of the ICM emission obtained with Resolve are  $z \lesssim 0.0095$ ; they are all significantly blueshifted relative to NGC 4696, indicating that the ICM is streaming towards us. In the central region, the bulk velocity relative to NGC 4696, estimated from the redshift, is  $v_{\text{bulk}} = -128 \pm 6 \text{ km s}^{-1}$  (Extended Data Table 1). The bulk velocity of the ICM varies spatially, showing the presence of a velocity gradient (Fig. 3a). In the NW and W regions, the bulk velocity is  $v_{\text{bulk}} = -179 \pm 21 \text{ km s}^{-1}$  and  $-197_{-17}^{+16} \text{ km s}^{-1}$ , respectively, and decreases to  $-305 \pm 17 \text{ km s}^{-1}$  in the SW region. The Mach number of the bulk flow is  $\mathcal{M} = 0.15$  for the hotter component and  $\mathcal{M} = 0.21$  for the cooler component in the central region and  $\mathcal{M} = 0.38$  in the SW region. We call this bulk gas motion “wind”.

Previous XMM-Newton observations with the pn-CCD showed a hint of blueshifted motion near the cluster centre, although the velocity uncertainties are large [9].

The emission lines of the metals that have contaminated the gas are also broadened, indicating the presence of turbulent motion. In our 5 studied regions, the velocity dispersion  $\sigma_v$  along the line of sight is systematically found to be less than  $120 \text{ km s}^{-1}$  (Fig. 3b; Extended Data Table 1), corresponding to a three-dimensional (3D) Mach number of  $\mathcal{M} \lesssim 0.25$  for  $T \sim 2.5 \text{ keV}$ . The ratio of kinetic to thermal energy density is  $\sim 0.03$ . The velocity dispersion is close to that estimated with the Chandra satellite from surface brightness variations ( $\sim 150 \text{ km s}^{-1}$  on  $\sim 35 \text{ kpc}$  scale at  $r \sim 23\text{--}50 \text{ kpc}$ ) [10]. In terms of 3D Mach number, the velocity dispersion in the Centaurus cluster is about half the mean value obtained for a sample of nearby giant elliptical galaxies using resonance scattering measured with the XMM-Newton Reflection Grating Spectrometer (RGS) [11]. The velocity dispersion is also smaller than that observed in the central region of the Perseus cluster with Hitomi ( $163 \pm 10 \text{ km s}^{-1}$ ) [12, 13], and it does not increase significantly even in the central region or in the AGN neighbourhood (Fig. 3b). This may indicate that the influence of the AGN on the ICM motion in the core is limited.

The increase in the absolute value of the bulk velocity  $|v_{\text{bulk}}|$  towards the southwest suggests that the source of the wind is not the AGN at the centre of NGC 4696. The sloshing of the core gas is a promising source of the wind since the motion induces the observed relative gas flow between the galaxy and the ICM [4, 14] when the direction of the oscillatory motion is nearly along the line of sight. The Centaurus cluster consists of the main component, including NGC 4696, called Cen 30, and a subgroup associated with NGC 4709 called Cen 45 [15]. The collision between Cen 30 and Cen 45 may have caused the sloshing. For example, the collision perturbs the position of NGC 4696, causing the galaxy to oscillate around the bottom of the gravitational potential well of the host cluster and sloshing the core gas. The wind in the core could also be induced by cosmological gas flows, including the large-scale velocity field produced by past cluster mergers, infalling galaxy groups and penetrating streams [16].

The heliocentric velocity and redshift of Cen 30 are  $V_{\text{Cen30}} = 3118 \pm 30 \text{ km s}^{-1}$  and  $z_{\text{Cen30}} = 0.01040$  [17], which are not much different from those of NGC 4696 ( $V_{\text{N4696}} = 3008 \pm 7 \text{ km s}^{-1}$  and  $z_{\text{N4696}} = 0.01003$ ); NGC 4696 is only slightly blueshifted by  $\sim 100 \text{ km s}^{-1}$  relative to Cen 30. If the sloshing is associated with the oscillation of NGC 4696, it may indicate that NGC 4696 is moving towards us in the cluster, approaching the turnaround point of its orbit, and slowing down relative to the cluster. Until the velocity decreases, the gas associated with the galaxy is confined by the ram pressure of the surrounding ICM, in addition to galactic gravity. However, as the galaxy approaches the turnaround point, the velocity of the galaxy and the density of the surrounding ICM decrease. As this reduces the ram pressure, the galactic gas is no longer confined and overruns the galaxy (“slingshot”; Fig. 4) [18–20]. Unlike the Perseus cluster, the Centaurus cluster does not show a prominent spiral density pattern in the X-ray image, which is produced when the galaxy oscillates with a small orbital angular momentum [19]. On the other hand, Fig. 1 shows that the cluster has a pair of density jumps (eastern and western cold fronts), suggesting that the line of sight is in the orbital plane and we may see the spiral pattern edge-on (Fig. 4) [19]. Fig. 3a

shows an east-west gradient in the bulk velocity, which may reflect the rotational motion associated with the spiral pattern. Previous work has shown a shift in the metal abundance distribution to the west [6], which is consistent with our picture of the projected gas distribution shifting to the west (Fig. 4).

The bulk velocity is particularly large in the circular structure called the “bay” in the Chandra image (Figs. 1 and 3a). Previous studies have suggested that the bay may be a Kelvin-Helmholtz instability roll [21]. However, if this is the case, there should be a strong gas flow brushing the bay in the plane of the sky, which is not clear from our observations. Alternatively, the bay could have been formed by a locally strong flow along the line of sight that washed away an old cavity created by AGN activity in the past.

The wind could help to suppress the development of massive cooling flows by shifting the flow centre away from the centre of NGC 4696. Indeed, Chandra observations have shown that the X-ray peak appears to be shifting  $\sim 1$  kpc away from the central AGN (Extended Data Fig. 2). This has been observed in other clusters as well [22]. The gradient of the bulk velocity and the deceleration of the core gas could excite Kelvin-Helmholtz and Rayleigh-Taylor instabilities, eventually leading to the formation of large eddies. The eddies could mix the gas and help prevent excessive cooling in the galaxy by transferring thermal energy from the surrounding hot ICM into the galaxy [3, 4]. The eddies could also distribute the locally injected energy from the central AGN and contribute to stable heating. Part of the kinetic energy of the wind could also be converted into thermal energy by the formation and decay of eddies. From the density distribution (Extended Data Fig. 3), the gas mass in the Resolve FOV is estimated to be  $\sim 10^{10} M_{\odot}$ . For a bulk velocity of  $|v_{\text{bulk}}| \sim 200 \text{ km s}^{-1}$ , the available kinetic energy is  $\sim 5 \times 10^{57}$  erg. We note that the typical duration of the wind cannot be too long since, otherwise, the metal abundance peak observed in the centre of NGC 4696 should have been blown away. Since the scale of the peak is  $R_p \sim 20$  kpc (Extended Data Fig. 3) and the wind speed is  $|v_{\text{bulk}}| \sim 200 \text{ km s}^{-1}$ , the duration should not be  $\gg R_p/|v_{\text{bulk}}| \sim 10^8$  yr. unless the direction of the gas flow is perfectly along the line of sight.

In contrast to the X-ray gas, the cold ( $\lesssim 100$  K) and warm ( $\sim 10^4$  K) gases detected in the central few kpc of NGC 4696 do not show the bulk motion relative to the galaxy [23–25]. Rather, they appear to rotate around the AGN in nearly the north-south direction at a speed of  $\sim 250\text{--}300 \text{ km s}^{-1}$  (Extended Data Fig. 4). Their unique motion, unrelated to the X-ray gas wind, suggests that these denser gases may have cooled from the hot X-ray gas and accumulated in the galactic centre before the wind began to blow. The rotational velocity of  $\sim 300 \text{ km s}^{-1}$  is probably much greater than the hot gas originally had since the velocity increases as the gas spirals down due to the conservation of angular momentum. Because the cold and warm phases are confined to the bottom of the galactic potential well, they are relatively immune to the wind. However, the outer part of the cold and warm gases can be blown away by the wind, preventing too much of it from being deposited in the galactic centre. The rotation of the cold and warm components is unlikely to have much effect on the wind motion of the X-ray gas because of their small volume filling factors.

The dissipation of turbulence is expected to heat the gas [26]. The turbulent heating rate in the gas with mass density  $\rho$  is  $Q_{\text{turb}} \sim 5 \rho \sigma_v^3 / l_t$ , where  $l_t$  is the length scale [26]. The radiative cooling rate of the gas is calculated from the gas density and the mean temperature  $T$ :  $Q_{\text{cool}} = n_e n_i \Lambda_n(T)$ , where  $n_e$  and  $n_i$  are the electron and ion number densities respectively, and  $\Lambda_n(T)$  is the normalised cooling function [27]. For the central region,  $\sigma_v \sim 117 \text{ km s}^{-1}$ ,  $l_t \sim 10\text{--}20$  kpc (the size of the bright region at the cluster centre or that of the central region in Fig. 1), the mean temperature  $T \sim 2$  keV and the metal abundance  $Z \sim 2$  solar (Extended Data Table 1), while  $\rho$ ,  $n_e$  and  $n_i$  are obtained from Chandra observations ( $n_e \sim 0.02 \text{ cm}^{-3}$ ; Extended Data Fig. 3). From these values we have  $Q_{\text{turb}}/Q_{\text{cool}} \sim 0.5\text{--}1.1$ , suggesting that the turbulent heating rate may be comparable to the radiative cooling rate, although this  $Q_{\text{turb}}$  estimate is only approximate. The high central Fe abundance value (Extended Data Fig. 3) indicates a very long metal accumulation time [28] and little AGN-induced perturbation. This is consistent with our conclusion that despite the presence of several generations of AGN-induced cavities indicating jet powers reaching  $\sim 2 \times 10^{43} \text{ erg s}^{-1}$  (see Extended Data Table 2), the kinematic influence of central AGN in the Centaurus cluster is not significant. For comparison, in the Perseus cluster, where the cavities were found to be associated with regions of increased turbulence [13], the estimated jet powers and total energies are at least an order of magnitude larger [e.g. 29].

Our results suggest that, at least on short timescales ( $\sim 10^8$  yr), the bulk gas motion induced by sloshing with coherent scales larger than  $\sim 14$  kpc (the typical region size in Fig. 1) plays a more important role in the thermal balance in the cluster core than the motion with scales smaller than  $\sim 14$  kpc induced by AGN cavities (Extended Data Fig. 2), which is observed by Resolve as line broadening or turbulence. Our results also support the idea that AGNs at the centre of clusters can be strongly influenced by external factors such as bulk gas motions. This should be taken into account when considering AGN feedback at cluster centres.

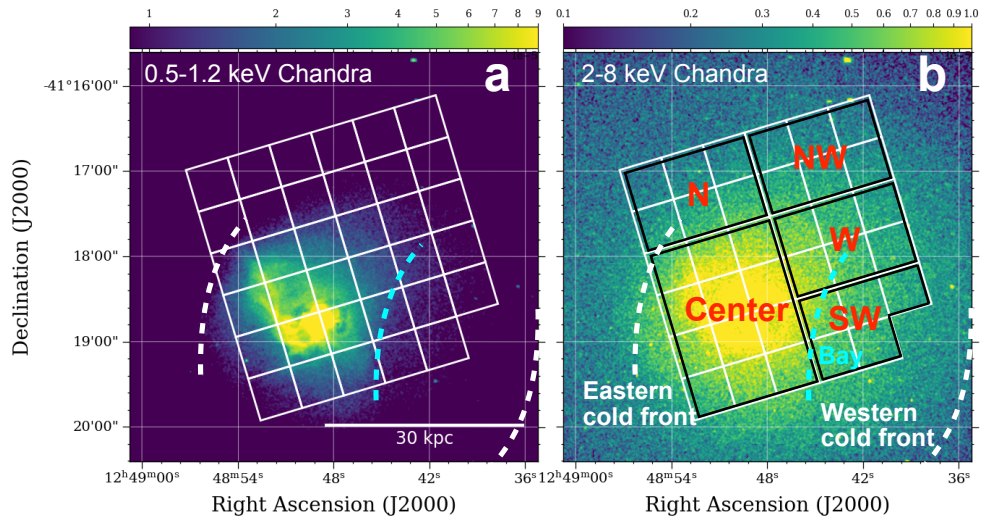


**Fig. 1** Resolve field of view (FOV) superimposed on the Chandra X-ray images at **a.** 0.5-1.2 keV and **b.** 2-8 keV. The red letters correspond to the regions extracted in the spectral analysis. The cyan dashed line indicates the "bay" structure, while the white dashed lines show the eastern and western cold fronts, respectively, as indicated in [6].

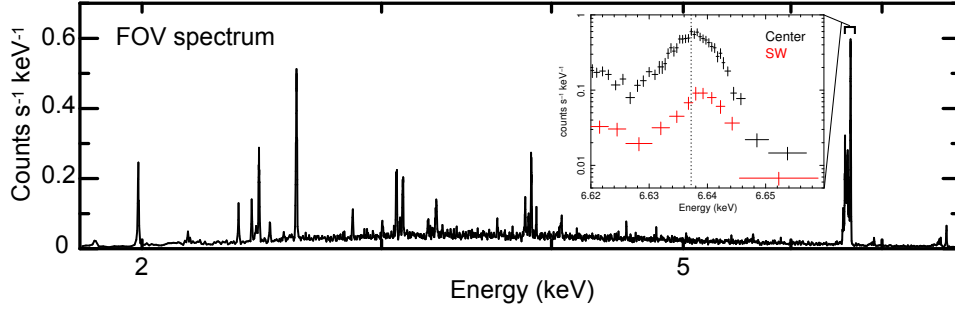


**Fig. 2** Resolve spectrum observed for the FOV in the 1.8–8.0 keV band. In the inset, Resolve spectra around the He- $\alpha$  Fe lines in 6.62–6.66 keV of the central and SW regions are shown in black and red, respectively. The vertical dotted black line indicates the central energy of the redshifted He- $\alpha$  Fe resonance line for the central region obtained in the SSM analysis. The peak of the SW spectrum is blueshifted with respect to the line.

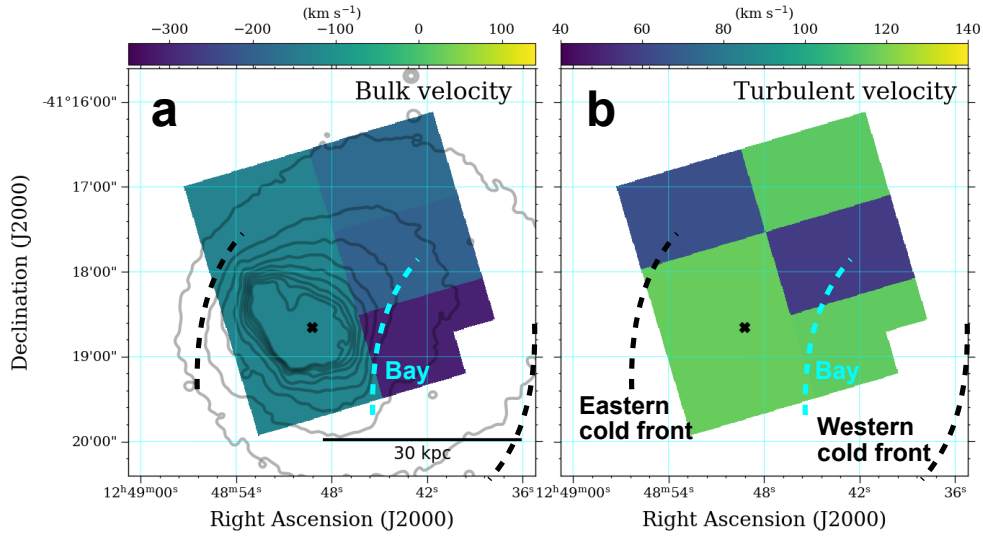


**Fig. 3** Maps for **a.** bulk and **b.** turbulent velocities. The positions of the AGN (marked by "X") and the "bay" are shown. The contour map of the Chandra X-ray image in 0.5–1.2 keV overlaid on the map **a.** The black and cyan dashed lines show the cold fronts and the bay, respectively, as in Fig. 1.

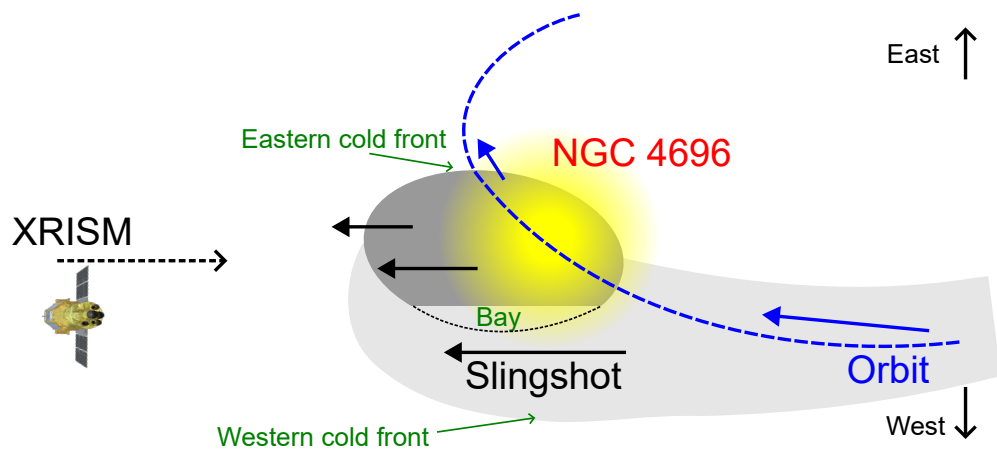


**Fig. 4** Schematic of the slingshot. An east-west cross-section of the cluster core is shown. The blue dashed line is the orbit of the stellar system of NGC 4696, shown in yellow. Dark and light grey indicate the denser and thinner gas initially associated with the galaxy. XRISM observes the system from the left.



# 1 Methods

## 1.1 XRISM Data reduction and analysis

The Resolve instrument onboard XRISM [30] is a system that combines an X-ray microcalorimeter spectrometer with an X-ray Mirror Assembly (XMA) to cover a  $3' \times 3'$  field of view (FOV). The microcalorimeter array is operated in a dewar in which a multi-stage cooling system maintains a stable environment at 50 mK. Resolve instrument was originally designed to cover the energy range between 0.3 and 12 keV, but only data in the  $E \gtrsim 2$  keV band were available during the Centaurus observation, because the Resolve dewar gate valve, which consists of a Be window and its support structure, was still closed at the time of the observation. In this paper, we use only the Resolve data to study the velocity structure of the Centaurus cluster core.

The Centaurus cluster observation data were processed using pre-pipeline software version "004\_001.15Oct2023\_Build7.011" and the processing (pipeline) script "03.00.011.008". In the following data analysis, the CALDB8 and `xa_rsl_rmparams_20190101v006.fits` were used to make the redistribution matrix files (RMFs) as is standard practice. The gain correction of Resolve was performed with  $^{55}\text{Fe}$  radioactive sources on the filter wheel (FW) and a total of 58 gain fiducial checks were performed during the observation, for  $\sim 30$  minutes once per orbit. The full width at half maximum (FWHM) of the composite Mn  $K\alpha$  spectrum of all pixels except for the calibration pixel (pixel 12) for the fiducial intervals was  $4.50 \pm 0.01$  eV. The FWHM energy resolution as a function of energy is given per pixel in the corresponding CALDB file, which is based on the initial analysis of PV phase calibration data. The uncertainty on the FWHM energy resolutions is estimated to be about 0.3 eV. The CALDB values of per-pixel FWHM energy resolution were used in the calculation of RMFs used for spectral analysis.

The energy scale accuracy after gain reconstruction has been shown to be 0.2 eV or better in-flight for a flat-field average in the band 5.4–8.0 eV using onboard calibration sources [31, 32]. Calibration measurements of the broad-band energy scale from 2 to 9 keV, in-flight, are consistent with an error of  $< \sim 1$  eV for a flat-field average. The Resolve instrument includes a calibration pixel that is part of the main detector but located just outside the instrument aperture that is constantly illuminated with a collimated  $^{55}\text{Fe}$  radioactive source. The calibration pixel can be used to assess the energy-scale reconstruction outside of the gain fiducial measurements by reconstructing its gain only during the gain fiducial intervals using the same method as the main array, but then fitting the calibration line only during the on-target intervals. For this observation, the calibration pixel gave an energy scale error of  $0.195 \pm 0.05$  eV at 5.9 keV, which is comparable to other XRISM observations. The gain scale error of 0.2 eV at 6 keV corresponds to a gas motion of  $\sim 10$  km  $\text{s}^{-1}$ , which is comparable to the statistical errors of bulk motion for the centre region of the observation and smaller than those for the other regions in our measurement. On the other hand, the error of about 0.3 eV in the LSF corresponds to the systematic uncertainty on the turbulent velocity of  $\sim 6$  km  $\text{s}^{-1}$  for 100 km  $\text{s}^{-1}$  if He-like Fe lines drive the spectral fits as a major factor of our analysis. If the spectral fits are determined by lower emission lines

around 2.5 keV such as sulfur lines, the systematic uncertainties are quite a bit higher ( $\sim 35 \text{ km s}^{-1}$  uncertainty for  $100 \text{ km s}^{-1}$ ), although a minor effect in our analysis.

Resolve events are classified as high-, medium-, and low-resolution (H, M, and L) grades based on the time proximity to a successive event in the same pixel, and further, they are subdivided into primary and secondary (p and s) classes depending on whether there is a triggered event after or before the event within a specific time interval [33]. The performance quoted here is for High-primary (Hp) events, the grade that was used in our analysis and which represents  $>98\%$  of the counts from this source. Finally, pixel 27, which is located in the “N” region in Fig. 1, has been shown to exhibit gain jumps of a few eV on time scales of a few hour scales, and thus is not currently recommended to be included in Resolve observations. However, in this early observation, gain fiducial measurements were made every 90 minutes, and the gain jumps were corrected. We, thus, used the full array for the spectral analysis of the entire observation.

We applied the standard event screening criteria [34, 35] for the Centaurus cluster observations, discarding time intervals of eclipses by Earth, small elevation angles from the sunlit Earth limb ( $< 20^\circ$ ), passing through the South Atlantic Anomaly, and the cryo-system recycling. This paper used only the Hp detector events (ITYPE = 0) for the spectral analysis. The non-X-ray background (NXB) spectra are estimated from the stacked Night Earth database (NXBDB) using the `rslnxbgen` task; then we applied the same screening as above, except for the threshold parameter of the dark Earth. We fitted the NXB spectra with an updated version of the Resolve NXB model reported in [35], and confirmed the instrumental line intensities. In the spectral fits, the NXB components were included as the model. Note that the Mn  $K\alpha$  line scattered from the collimated  $^{55}\text{Fe}$  source for the calibration pixel is non-uniformly distributed across the array, and care should be taken in treating subarray regions until more NXBDB statistics are available. However, the NXB contribution has a small impact on determining the central energy of emission lines and the line width on our spectral analysis as shown in Fig. 1. We created the RMFs using the extra-large mode option in the `rslmkrmf` task to represent the spectral shape in the lower and higher energy bands, including the escape peak and electron loss continuum effects. We also created ancillary responses (ARFs) for the spectrum of each region. The ARFs were appropriate for the diffuse emission from the ICM and were based on the X-ray image observed with Chandra in the 2–8 keV energy band using the `xaarfgen` task. Finally, the spectra were grouped so that each bin had at least 1 count to fit the spectra using the C-statistic method [36] without subtracting any background emissions.

Here, the ICM emissions in each region were reproduced by one or two thermal plasma models (bvapex model with AtomDB version 3.0.9 in the XSPEC package). The HPD of Resolve XMA is  $1.3'$ , thus contamination from adjacent regions must be considered. This effect is taken into account in the SSM analysis, and the amount of leakage into each region is evaluated by the ARFs of each region produced using ray-tracing, taking into account the shape of the Point Spread Function (PSF). We note that the X-ray spectrum in a region includes photons from neighbouring regions due to the PSF of the XMA and the small wobbling effect of attitude. To take this spatial-spectral mixing effect into account, we calculated flux contribution from one region

( $B$ ) to another or itself ( $A$ ). This was done by ray-trace calculations simulating paths of incident photons to the focal plane passing through the XMA with the `xrtraytrace` task, where photons reach an area on the detector, corresponding to  $A$  on the sky, from the assumed source by the Chandra image of  $B$ . Then, the fitting model on  $A$  is estimated with contributions from all regions as  $M_A = \text{RMF}_A \otimes \sum M_B \text{ARF}_{B \rightarrow A}$  ([13] for more details). According to ray-tracing calculations, the leakage from the central region to the SW region is equivalent to  $\sim 20\%$  of the SW region, and about half of the total flux in the SW region would come from the other regions. Therefore, it is taken into account in the SSM analysis. The velocity difference between the centre and SW regions is  $|v| \sim 110 \text{ km s}^{-1}$  when the spectra for only each region were fitted independently, without the SSM analysis, but it emphasizes the velocity difference more. We provide representative spectra and best-fitting models with the SSM analysis in Extended Data Fig. 1. The derived parameters are summarised in Extended Data Table 1. As for the systematic error of this SSM analysis, Hayashi and *et al.* [37] reports that when the point-like source was on-axis, the difference between observed count rates and those predicted by ground data was less than 20% for most pixels (although much larger for some pixels) and when it was  $1.8'$  off-axis, the difference was less than 50% for each pixel [37, 38]. The differences between observed count rates per pixel and those predicted by the XMA model in the CALDB and are somewhat larger than the differences between inflight and ground data. In our case, since the Centaurus cluster are diffuse source, it is difficult to evaluate, but we have investigated the impact of the PSF contamination by artificially shifting the input Chandra image for the ARF calculations by  $10''$  in the on-axis or off-axis direction to investigate the systematic error. Since the difference between the results obtained here and those in Table 1 was less than the statistical errors, we evaluated these systematic errors to be less than the statistical errors, and it does not affect our results. All the abundances are expressed using the proto-Solar values [39]. A foreground absorption column was fixed at  $7.77 \times 10^{20} \text{ cm}^{-2}$  [40]. We have ensured that the X-ray emission from the central AGN does not affect our results by using the upper limit of the flux [41]. We adopted the heliocentric correction of  $24 \text{ km s}^{-1}$ .

## 1.2 Redshift determination

The Centaurus cluster has two main subclusters, Cen 30 and Cen 45 [17]. NGC 4696 is the central galaxy of the Cen 30 subcluster. The redshift of the Cen 30 subcluster has been constrained to  $z=0.0104$ , or the velocity of  $3118 \pm 30 \text{ km s}^{-1}$  [17]. We also used the Multi-Unit Spectroscopic Explorer (MUSE) data of NGC 4696 to determine its velocity from stellar absorption lines. Twenty-two MUSE observations from 2014 to 2023 were used, with a total exposure time of 5.66 hours, under seeing conditions of  $0.70''$ – $1.21''$  and airmass of 1.08–1.72. For each pointing, we used the MUSE pipeline (version 2.9.0) with the ESO Recipe Execution Tool (EsoRex) to reduce the raw data, which provides a standard procedure to calibrate the individual exposures and combine them into a datacube. Further sky subtraction was performed with the Zurich Atmosphere Purge software (ZAP). We extracted the MUSE spectrum within the central 1 kpc radius and fit it with pPXF. The derived heliocentric stellar velocity is

$3008 \pm 7 \text{ km s}^{-1}$ . We also examined the spectrum within the central 4 kpc radius, with the same stellar velocity derived.

### 1.3 Complementary Chandra observations

We leveraged the great spatial resolution of the Chandra X-ray observatory to perform a complementary spatially-resolved image and spectral analysis of the Centaurus cluster. For the analysis, we used 15 archival Chandra observations with a total cleaned exposure time of 777.4 ks. All Chandra OBSIDs were processed using the `chandra_repro` script, reprojected, and merged. The point sources were detected using the `wavdetect` procedure (ECF = 0.9, threshold =  $10^{-5}$ ), and the background light curves in the 0.5–7.0 keV band were extracted and deflared using the `deflare` routine ( $3\sigma$  clipping level).

For the spatially resolved spectral analysis, we limited our analysis to only 13 observations with the ACIS-S3 chip centred at the central galaxy, NGC 4696. Using the `specextract` procedure, we produced spectra for 24 concentric annuli centred at the position of the AGN with the outermost annulus of 300 arcsec, where background spectral files for each annulus were extracted from blank-sky backgrounds. The spectral modelling was performed using PyXspec v2.1.3 package (XSPEC 12.13.1 [42]). The thermodynamic profiles were obtained by fitting a single temperature `apec` model absorbed by the photoelectric absorption (`phabs`). The deprojection was performed using the `project` multiplicative model component assuming a spherical symmetry. In addition, we included a power-law model component with a photon index of 1.9 [43] to describe the emission of the central AGN in the innermost annulus and in outer annuli with a photon index of  $\Gamma = 1.56$  [44] to account for unresolved point sources. The model for each annulus is identical and is defined as follows:

$$\text{project}(\text{phabs}(\text{apec})) + \text{phabs}(\text{powerlaw})$$

The temperatures and metal abundances of individual annuli were allowed to vary. However, for some of the annuli, we tied parameters for 2 or more neighbouring annuli together (see Extended Data Fig. 3) to constrain these parameters with a relative uncertainty smaller than 25 percent. The fitting was performed in the broad energy band (0.55–7.0 keV) as well as only in the hard band (1.8–7.0 keV), which is more similar to XRISM Resolve spectra. During the fitting, the redshift was fixed to  $z = 0.01040$ , and the galactic hydrogen column was fixed to the value of  $N_H = 7.77 \times 10^{20} \text{ cm}^{-2}$  [40], however, even after thawing the parameter we obtained consistent results. The background files were treated using the `wstat` statistics (modified `cstat`; [36]). For the analysis of the Chandra data, we assumed the standard flat  $\Lambda$ CDM cosmology, with  $H_0 = 70 \text{ km s}^{-1} \text{ Mpc}^{-1}$ ,  $q_0 = 0$ ,  $\Omega_{\Lambda,0} = 0.73$ . All the abundances are expressed with respect to proto-Solar values [39]. The uncertainties are expressed in the  $1\sigma$  credible interval and were estimated from posterior distributions obtained from MCMC simulations.

Furthermore, we generated the merged images in the broad energy band (0.5–7.0 keV) as well as in individual sub-bands: soft (0.5–1.2 keV), medium (1.2–2 keV), and hard (2.0–7 keV). We filled the point sources in these images using the `dmfilth`

routine and exposure-corrected them with weighted exposure maps. We then used these images to identify individual spatial structures such as cold fronts, X-ray cavities, etc. Because the soft energy band is dominated by the filament-like sub-structure, X-ray cavities were detected mainly based on the hard-band image (we also tested other sub-bands, e.g. 1.5–7 keV or 2.5–7 keV, but the obtained results were consistent). For detecting the X-ray cavities, we used the Cavity Detection Tool [45]. The CADET pipeline successfully detected the previously known central cavity pair (Generation 1). On top of that, the pipeline discovered an older generation of cavities in the NE-SW direction (Generation 2) and potentially an even older but non-significant<sup>1</sup> generation of cavities in the SE-W direction (Generation 3) (Extended Data Fig. 2). The total energy stored in the detected X-ray cavities and the corresponding mechanical jet powers were estimated by combining the cavity extent estimated with CADET and temperature and density profiles obtained from the spatially-resolved spectral analysis of Chandra data (Extended Data Table 2). Including the energy released by the potential Generation 3 X-ray cavities, the total energy released into the hot atmosphere of NGC4696 in the last 15 Myr is approximately  $\sim 6 \times 10^{57}$  erg (or  $\sim 4 \times 10^{57}$  erg in last 12 Myr in the case of 2 latest cavity generations).

---

<sup>1</sup>Significance of obtained cavity detections were tested using azimuthal and radial surface-brightness profiles [for more info, see 45].

## References

- [1] Churazov, E., Sunyaev, R., Forman, W., Böhringer, H.: Cooling flows as a calorimeter of active galactic nucleus mechanical power. *Mon. Not. R. Astron. Soc.* **332**(3), 729–734 (2002) <https://doi.org/10.1046/j.1365-8711.2002.05332.x> [arXiv:astro-ph/0201125](https://arxiv.org/abs/astro-ph/0201125) [astro-ph]
- [2] McNamara, B.R., Nulsen, P.E.J.: Heating Hot Atmospheres with Active Galactic Nuclei. *Annu. Rev. Astron. Astrophys.* **45**(1), 117–175 (2007) <https://doi.org/10.1146/annurev.astro.45.051806.110625> [arXiv:0709.2152](https://arxiv.org/abs/0709.2152) [astro-ph]
- [3] Fujita, Y., Matsumoto, T., Wada, K.: Strong Turbulence in the Cool Cores of Galaxy Clusters: Can Tsunamis Solve the Cooling Flow Problem? *Astrophys. J.* **612**(1), 9–12 (2004) <https://doi.org/10.1086/424483> [arXiv:astro-ph/0407368](https://arxiv.org/abs/astro-ph/0407368) [astro-ph]
- [4] ZuHone, J.A., Markevitch, M., Johnson, R.E.: Stirring Up the Pot: Can Cooling Flows in Galaxy Clusters be Quenched by Gas Sloshing? *Astrophys. J.* **717**(2), 908–928 (2010) <https://doi.org/10.1088/0004-637X/717/2/908> [arXiv:0912.0237](https://arxiv.org/abs/0912.0237) [astro-ph.CO]
- [5] Blakeslee, J.P., Lucey, J.R., Barris, B.J., Hudson, M.J., Tonry, J.L.: A synthesis of data from fundamental plane and surface brightness fluctuation surveys. *Mon. Not. R. Astron. Soc.* **327**(3), 1004–1020 (2001) <https://doi.org/10.1046/j.1365-8711.2001.04800.x> [arXiv:astro-ph/0108194](https://arxiv.org/abs/astro-ph/0108194) [astro-ph]
- [6] Sanders, J.S., *et al.*: A very deep Chandra view of metals, sloshing and feedback in the Centaurus cluster of galaxies. *Mon. Not. R. Astron. Soc.* **457**(1), 82–109 (2016) <https://doi.org/10.1093/mnras/stv2972> [arXiv:1601.01489](https://arxiv.org/abs/1601.01489) [astro-ph.GA]
- [7] Tashiro, M., *et al.*: Development and operation status of X-Ray Imaging and Spectroscopy Mission (XRISM). In: Herder, J.-W.A., Nikzad, S., Nakazawa, K. (eds.) *Space Telescopes and Instrumentation 2024: Ultraviolet to Gamma Ray*, vol. 13093, p. 130931. SPIE (2024). <https://doi.org/10.1117/12.3019325>. International Society for Optics and Photonics. <https://doi.org/10.1117/12.3019325>
- [8] Fujita, Y., *et al.*: The correlation between the 500 pc scale molecular gas masses and AGN powers for massive elliptical galaxies. *Publ. Astron. Soc. Jpn* **75**(5), 925–936 (2023) <https://doi.org/10.1093/pasj/psad050> [arXiv:2303.16927](https://arxiv.org/abs/2303.16927) [astro-ph.GA]
- [9] Gatuzz, E., *et al.*: The velocity structure of the intracluster medium of the Centaurus cluster. *Mon. Not. R. Astron. Soc.* **513**(2), 1932–1946 (2022) <https://doi.org/10.1093/mnras/stac846> [arXiv:2203.12635](https://arxiv.org/abs/2203.12635) [astro-ph.CO]
- [10] Zhuravleva, I., Allen, S.W., Mantz, A., Werner, N.: Gas Perturbations in the Cool

- Cores of Galaxy Clusters: Effective Equation of State, Velocity Power Spectra, and Turbulent Heating. *Astrophys. J.* **865**(1), 53 (2018) <https://doi.org/10.3847/1538-4357/aadae3> [arXiv:1707.02304](https://arxiv.org/abs/1707.02304) [astro-ph.HE]
- [11] Ogorzalek, A., *et al.*: Improved measurements of turbulence in the hot gaseous atmospheres of nearby giant elliptical galaxies. *Mon. Not. R. Astron. Soc.* **472**(2), 1659–1676 (2017) <https://doi.org/10.1093/mnras/stx2030> [arXiv:1702.04364](https://arxiv.org/abs/1702.04364) [astro-ph.HE]
- [12] Hitomi Collaboration: The quiescent intracluster medium in the core of the Perseus cluster. *Nature* **535**(7610), 117–121 (2016) <https://doi.org/10.1038/nature18627> [arXiv:1607.04487](https://arxiv.org/abs/1607.04487) [astro-ph.GA]
- [13] Hitomi Collaboration: Atmospheric gas dynamics in the Perseus cluster observed with Hitomi. *Publ. Astron. Soc. Jpn* **70**(2), 9 (2018) <https://doi.org/10.1093/pasj/psx138> [arXiv:1711.00240](https://arxiv.org/abs/1711.00240) [astro-ph.HE]
- [14] Markevitch, M., Vikhlinin, A., Mazzotta, P.: Nonhydrostatic Gas in the Core of the Relaxed Galaxy Cluster A1795. *Astrophys. J.* **562**(2), 153–156 (2001) <https://doi.org/10.1086/337973> [arXiv:astro-ph/0108520](https://arxiv.org/abs/astro-ph/0108520) [astro-ph]
- [15] Lucey, J.R., Currie, M.J., Dickens, R.J.: The Centaurus cluster of galaxies - II. The bimodal velocity structure. *Mon. Not. R. Astron. Soc.* **221**, 453–472 (1986) <https://doi.org/10.1093/mnras/221.2.453>
- [16] Lau, E.T., Gaspari, M., Nagai, D., Coppi, P.: Physical Origins of Gas Motions in Galaxy Cluster Cores: Interpreting Hitomi Observations of the Perseus Cluster. *Astrophys. J.* **849**(1), 54 (2017) <https://doi.org/10.3847/1538-4357/aa8c00> [arXiv:1705.06280](https://arxiv.org/abs/1705.06280) [astro-ph.CO]
- [17] Veronica, A., *et al.*: The SRG/eROSITA All-Sky Survey: Large-scale view of the Centaurus cluster. *arXiv e-prints*, 2404–04909 (2024) <https://doi.org/10.48550/arXiv.2404.04909> [arXiv:2404.04909](https://arxiv.org/abs/2404.04909) [astro-ph.CO]
- [18] Hallman, E.J., Markevitch, M.: Chandra Observation of the Merging Cluster A168: A Late Stage in the Evolution of a Cold Front. *Astrophys. J.* **610**(2), 81–84 (2004) <https://doi.org/10.1086/423449> [arXiv:astro-ph/0406322](https://arxiv.org/abs/astro-ph/0406322) [astro-ph]
- [19] Ascasibar, Y., Markevitch, M.: The Origin of Cold Fronts in the Cores of Relaxed Galaxy Clusters. *Astrophys. J.* **650**(1), 102–127 (2006) <https://doi.org/10.1086/506508> [arXiv:astro-ph/0603246](https://arxiv.org/abs/astro-ph/0603246) [astro-ph]
- [20] Sheardown, A., *et al.*: A New Class of X-Ray Tails of Early-type Galaxies and Sub-clusters in Galaxy Clusters: Slingshot Tails versus Ram Pressure Stripped Tails. *Astrophys. J.* **874**(2), 112 (2019) <https://doi.org/10.3847/1538-4357/ab0c06> [arXiv:1903.00482](https://arxiv.org/abs/1903.00482) [astro-ph.GA]

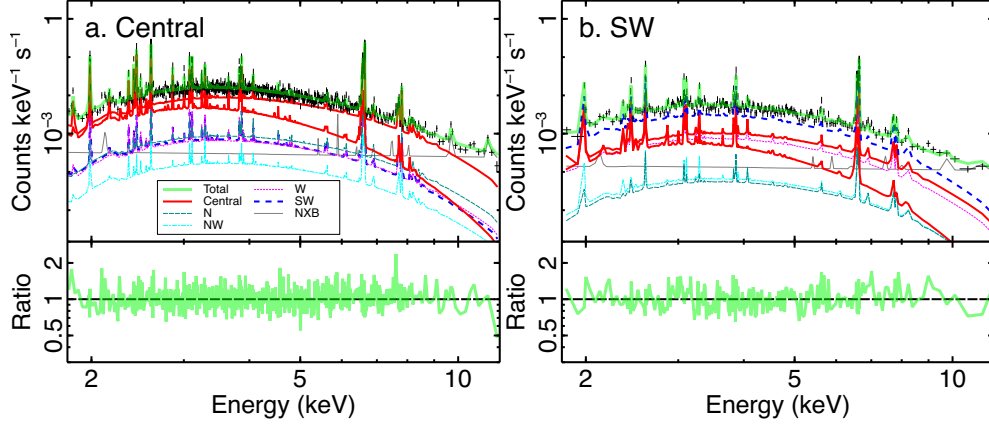


- [21] Walker, S.A., *et al.*: Is there a giant Kelvin-Helmholtz instability in the sloshing cold front of the Perseus cluster? *Mon. Not. R. Astron. Soc.* **468**(2), 2506–2516 (2017) <https://doi.org/10.1093/mnras/stx640> arXiv:1705.00011 [astro-ph.CO]
- [22] Werner, N., *et al.*: Deep Chandra study of the truncated cool core of the Ophiuchus cluster. *Mon. Not. R. Astron. Soc.* **460**(3), 2752–2764 (2016) <https://doi.org/10.1093/mnras/stw1171> arXiv:1604.01038 [astro-ph.CO]
- [23] Mittal, R., *et al.*: Herschel observations of the Centaurus cluster - the dynamics of cold gas in a cool core. *Mon. Not. R. Astron. Soc.* **418**(4), 2386–2402 (2011) <https://doi.org/10.1111/j.1365-2966.2011.19634.x> arXiv:1108.2757 [astro-ph.CO]
- [24] Canning, R.E.A., *et al.*: A deep spectroscopic study of the filamentary nebulosity in NGC 4696, the brightest cluster galaxy in the Centaurus cluster. *Mon. Not. R. Astron. Soc.* **417**(4), 3080–3099 (2011) <https://doi.org/10.1111/j.1365-2966.2011.19470.x> arXiv:1107.4011 [astro-ph.CO]
- [25] Olivares, V., *et al.*: Ubiquitous cold and massive filaments in cool core clusters. *Astron. Astrophys.* **631**, 22 (2019) <https://doi.org/10.1051/0004-6361/201935350> arXiv:1902.09164 [astro-ph.GA]
- [26] Zhuravleva, I., *et al.*: Turbulent heating in galaxy clusters brightest in X-rays. *Nature* **515**(7525), 85–87 (2014) <https://doi.org/10.1038/nature13830> arXiv:1410.6485 [astro-ph.HE]
- [27] Sutherland, R.S., Dopita, M.A.: Cooling Functions for Low-Density Astrophysical Plasmas. *Astrophys. J.* **88**, 253 (1993) <https://doi.org/10.1086/191823>
- [28] Böhringer, H., Matsushita, K., Churazov, E., Finoguenov, A., Ikebe, Y.: Implications of the central metal abundance peak in cooling core clusters of galaxies. *Astron. Astrophys.* **416**, 21–25 (2004) <https://doi.org/10.1051/0004-6361:20040047> arXiv:astro-ph/0402216 [astro-ph]
- [29] Rafferty, D.A., McNamara, B.R., Nulsen, P.E.J., Wise, M.W.: The Feedback-regulated Growth of Black Holes and Bulges through Gas Accretion and Starbursts in Cluster Central Dominant Galaxies. *Astrophys. J.* **652**(1), 216–231 (2006) <https://doi.org/10.1086/507672> arXiv:astro-ph/0605323 [astro-ph]
- [30] Ishisaki, Y., *et al.*: Status of resolve instrument onboard X-Ray Imaging and Spectroscopy Mission (XRISM). In: den Herder, J.-W.A., Nikzad, S., Nakazawa, K. (eds.) *Space Telescopes and Instrumentation 2022: Ultraviolet to Gamma Ray*. Society of Photo-Optical Instrumentation Engineers (SPIE) Conference Series, vol. 12181, p. 121811 (2022). <https://doi.org/10.1117/12.2630654>
- [31] Porter, F.S., *et al.*: In-flight performance of the XRISM/Resolve detector system. In: Herder, J.-W.A., Nikzad, S., Nakazawa, K. (eds.) *Space Telescopes and Instrumentation 2024: Ultraviolet to Gamma Ray*, vol. 13093, p. 130931. SPIE



- (2024). <https://doi.org/10.1117/12.3018882> . International Society for Optics and Photonics. <https://doi.org/10.1117/12.3018882>
- [32] Eckart, M.E., *et al.*: Energy gain scale calibration of the XRISM Resolve microcalorimeter spectrometer: ground calibration results and on orbit comparison. In: Herder, J.-W.A., Nikzad, S., Nakazawa, K. (eds.) Space Telescopes and Instrumentation 2024: Ultraviolet to Gamma Ray, vol. 13093, p. 130931. SPIE (2024). <https://doi.org/10.1117/12.3019276> . International Society for Optics and Photonics. <https://doi.org/10.1117/12.3019276>
- [33] Ishisaki, Y., *et al.*: In-flight performance of pulse-processing system of the ASTRO-H/Hitomi soft x-ray spectrometer. *Journal of Astronomical Telescopes, Instruments, and Systems* **4**, 011217 (2018) <https://doi.org/10.1117/1.JATIS.4.1.011217>
- [34] Kilbourne, C.A., *et al.*: In-flight calibration of Hitomi Soft X-ray Spectrometer. (1) Background. *Publ. Astron. Soc. Jpn* **70**(2), 18 (2018) <https://doi.org/10.1093/pasj/psx139>
- [35] XRISM Collaboration: The XRISM First Light Observation: Velocity Structure and Thermal Properties of the Supernova Remnant N132D. arXiv e-prints, 2408–14301 (2024) <https://doi.org/10.48550/arXiv.2408.14301> arXiv:2408.14301 [astro-ph.HE]
- [36] Cash, W.: Parameter estimation in astronomy through application of the likelihood ratio. *Astrophys. J.* **228**, 939–947 (1979) <https://doi.org/10.1086/156922>
- [37] Hayashi, T., *et al.*: In-orbit performance of the XMA for XRISM/Resolve. In: Herder, J.-W.A., Nikzad, S., Nakazawa, K. (eds.) Space Telescopes and Instrumentation 2024: Ultraviolet to Gamma Ray, vol. 13093, p. 130931. SPIE (2024). <https://doi.org/10.1117/12.3019600> . International Society for Optics and Photonics. <https://doi.org/10.1117/12.3019600>
- [38] Tamura, K., *et al.*: In-orbit performance of the Xtend-XMA onboard XRISM. In: Herder, J.-W.A., Nikzad, S., Nakazawa, K. (eds.) Space Telescopes and Instrumentation 2024: Ultraviolet to Gamma Ray, vol. 13093, p. 130931. SPIE (2024). <https://doi.org/10.1117/12.3020109> . International Society for Optics and Photonics. <https://doi.org/10.1117/12.3020109>
- [39] Lodders, K., Palme, H., Gail, H.-P.: Abundances of the Elements in the Solar System. *Landolt B&ouml;rnsstein* **4B**, 712 (2009) [https://doi.org/10.1007/978-3-540-88055-4\\_34](https://doi.org/10.1007/978-3-540-88055-4_34) arXiv:0901.1149 [astro-ph.EP]
- [40] HI4PI Collaboration: HI4PI: A full-sky H I survey based on EBHIS and GASS. *Astron. Astrophys.* **594**, 116 (2016) <https://doi.org/10.1051/0004-6361/201629178> arXiv:1610.06175 [astro-ph.GA]

- [41] Taylor, G.B., Sanders, J.S., Fabian, A.C., Allen, S.W.: The low-power nucleus of PKS 1246-410 in the Centaurus cluster. *Mon. Not. R. Astron. Soc.* **365**(3), 705–711 (2006) <https://doi.org/10.1111/j.1365-2966.2005.09705.x> arXiv:astro-ph/0510247 [astro-ph]
- [42] Arnaud, K.A.: XSPEC: The First Ten Years. In: Jacoby, G.H., Barnes, J. (eds.) *Astronomical Data Analysis Software and Systems V*. Astronomical Society of the Pacific Conference Series, vol. 101, p. 17 (1996)
- [43] Gilli, R., Comastri, A., Hasinger, G.: The synthesis of the cosmic X-ray background in the Chandra and XMM-Newton era. *Astron. Astrophys.* **463**(1), 79–96 (2007) <https://doi.org/10.1051/0004-6361:20066334> arXiv:astro-ph/0610939 [astro-ph]
- [44] Irwin, J.A., Athey, A.E., Bregman, J.N.: X-Ray Spectral Properties of Low-Mass X-Ray Binaries in Nearby Galaxies. *Astrophys. J.* **587**(1), 356–366 (2003) <https://doi.org/10.1086/368179> arXiv:astro-ph/0212422 [astro-ph]
- [45] Plšek, T., Werner, N., Topinka, M., Simionescu, A.: CAvity DEtection Tool (CADET): pipeline for detection of X-ray cavities in hot galactic and cluster atmospheres. *Monthly Notices of the Royal Astronomical Society* **527**(2), 3315–3346 (2023) <https://doi.org/10.1093/mnras/stad3371> <https://academic.oup.com/mnras/article-pdf/527/2/3315/53668373/stad3371.pdf>



**Extended Data Fig. 1** Representative spectra from the **a.** Central and **b.** SW regions and the best-fitting models, including the SSM effect. The total models are shown as a transparent green thick solid line. The grey thin solid lines are for NXB. We also show the contributions from the central (red thick solid), N (dark green thin dashed), NW (cyan thin dashed), W (magenta thin dashed) and SW (blue thick dashed) regions. As the central region has two temperature components, there are two red thick solid lines in each figure.

**Extended Data Table 1** Parameters for regions shown in Fig. 1 obtained with Resolve.

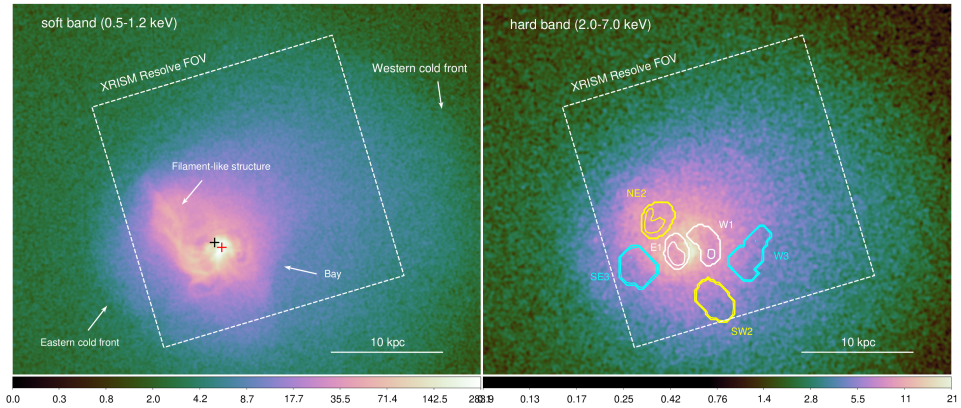
Region <sup>1</sup>	Temperature (keV)	Fe Abundance (Solar)	Bulk Velocity <sup>3</sup> (km s <sup>-1</sup> )	Turbulent Velocity (km s <sup>-1</sup> )
Central <sup>2</sup>	2.81 <sup>+0.18</sup> <sub>-0.20</sub> / 1.41 <sup>+0.20</sup> <sub>-0.10</sub>	1.65 <sup>+0.07</sup> <sub>-0.07</sub>	-128 <sup>+6.3</sup> <sub>-6.3</sub>	117 <sup>+9</sup> <sub>-9</sub>
N	3.10 <sup>+0.15</sup> <sub>-0.14</sub>	1.31 <sup>+0.12</sup> <sub>-0.11</sub>	-132 <sup>+14</sup> <sub>-14</sub>	64 <sup>+27</sup> <sub>-33</sub>
NW	2.91 <sup>+0.15</sup> <sub>-0.15</sub>	1.34 <sup>+0.15</sup> <sub>-0.14</sub>	-179 <sup>+21</sup> <sub>-21</sub>	115 <sup>+29</sup> <sub>-31</sub>
W	2.55 <sup>+0.11</sup> <sub>-0.12</sub>	1.54 <sup>+0.20</sup> <sub>-0.17</sub>	-197 <sup>+16</sup> <sub>-17</sub>	58 <sup>+35</sup> <sub>-50</sub>
SW	2.38 <sup>+0.14</sup> <sub>-0.09</sub>	2.04 <sup>+0.21</sup> <sub>-0.20</sub>	-305 <sup>+17</sup> <sub>-17</sub>	116 <sup>+20</sup> <sub>-19</sub>

Note: For this simultaneous fit,  $C$ -stat is 23637.16 with 28488 degrees of freedom.

<sup>1</sup>Errors indicate 1 sigma confidence level and correspond only to statistical errors in the spectral fit.

<sup>2</sup>Two temperature model.

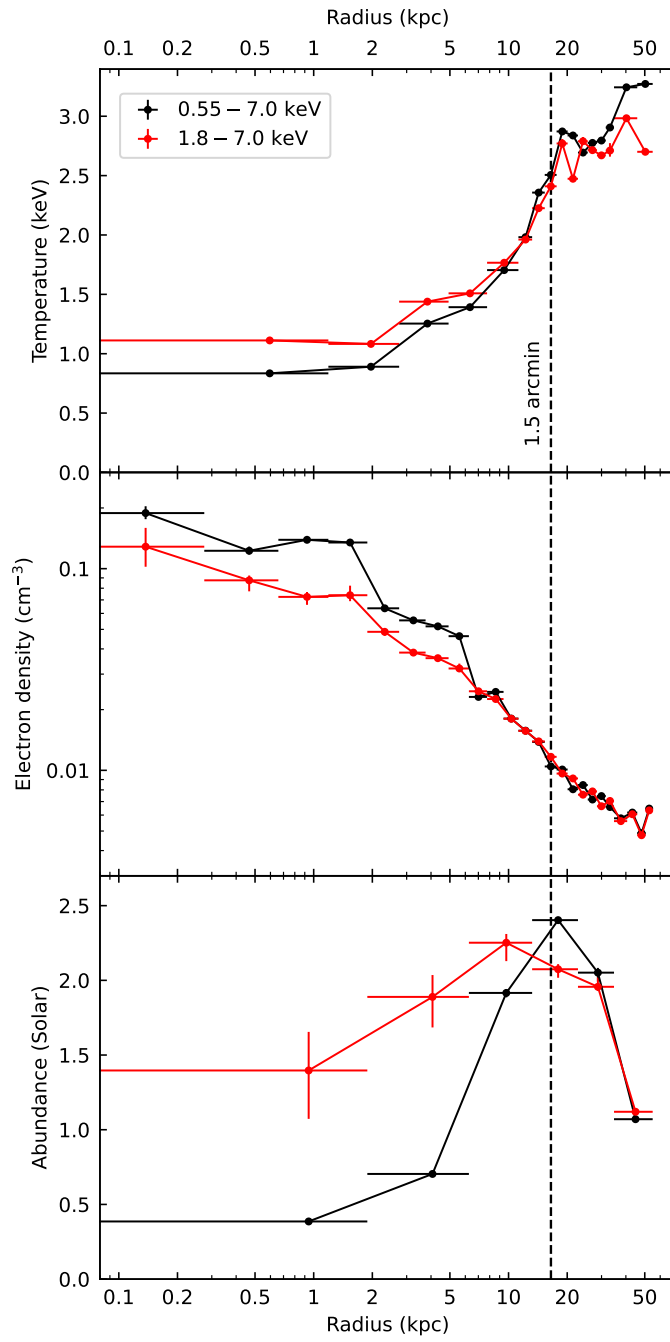
<sup>3</sup>Heliocentric velocity relative to 3008 km s<sup>-1</sup>. The heliocentric velocity of NGC 4696 is 3008 ± 7 km s<sup>-1</sup>.



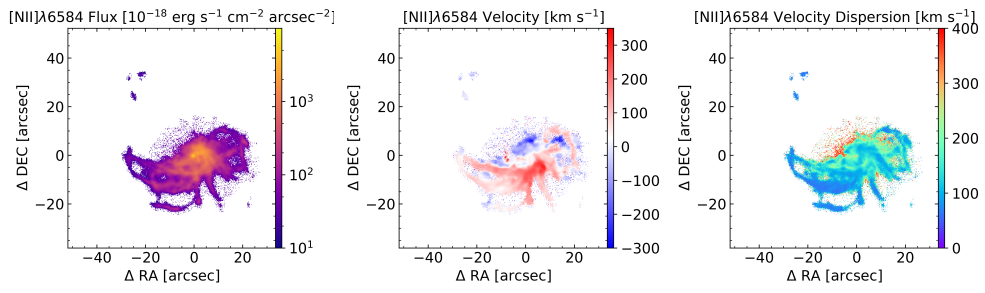
**Extended Data Fig. 2** **Left:** Soft band (0.5 – 1.2 keV) Chandra image with main features highlighted. The white dashed line shows the XRISM Resolve FOV. The black cross indicates the position of the central AGN of galaxy NGC4696 separated by  $\sim 1$  kpc from the X-ray peak of the Centaurus cluster (red cross). **Right:** Hard band (2.0 – 7.0 keV) Chandra image with superimposed contours of CADET cavity predictions for individual detected cavity generations.

**Extended Data Table 2** Properties of individual cavity generations detected in the core of the Centaurus cluster: total deposited energy  $E$ , and the corresponding mechanical power of the jet  $P_{\text{jet}}$ .

Cavities	$E$ (erg)	$P_{\text{jet}}$ ( $\text{erg s}^{-1}$ )
E1–W1	$1.3^{+1.4}_{-0.7} \times 10^{57}$	$1.9^{+1.3}_{-0.8} \times 10^{43}$
NE2–SW2	$2.5^{+1.5}_{-1.0} \times 10^{57}$	$8.5^{+6.1}_{-3.7} \times 10^{42}$
SE3–W3	$2.0^{+1.2}_{-0.8} \times 10^{57}$	$4.5^{+2.7}_{-1.9} \times 10^{42}$



**Extended Data Fig. 3** Temperature, electron density, and metal abundance profiles obtained from deprojection analysis of broad (black points) and hard (red points) band Chandra data.



**Extended Data Fig. 4** Flux, velocity, and velocity dispersion maps of the warm, ionized gas at the centre of NGC 4696, traced by the strongest optical line [N II]  $\lambda 6584$  from the *MUSE* data. The nucleus is at the (0, 0) position. The velocity is relative to the system velocity of 3008 km/s.

**Acknowledgements** This work was supported by JSPS KAKENHI grant numbers JP22H00158, JP22H01268, JP22K03624, JP23H04899, JP21K13963, JP24K00638, JP24K17105, JP21K13958, JP21H01095, JP23K20850, JP24H00253, JP21K03615, JP24K00677, JP20K14491, JP23H00151, JP19K21884, JP20H01947, JP20KK0071, JP23K20239, JP24K00672, JP24K17104, JP24K17093, JP20K04009, JP21H04493, JP20H01946, JP23K13154, JP19K14762, JP20H05857, and JP23K03459, and NASA grant numbers 80NSSC23K0650, 80NSSC20K0733, 80NSSC18K0978, 80NSSC20K0883, 80NSSC20K0737, 80NSSC24K0678, 80NSSC18K1684, and 80NSSC22K1922. LC acknowledges support from NSF award 2205918. CD acknowledges support from STFC through grant ST/T000244/1. LG acknowledges financial support from Canadian Space Agency grant 18XARMSTMA. AT and the present research are in part supported by the Kagoshima University postdoctoral research program (KU-DREAM). SY acknowledges support by the RIKEN SPDR Program. IZ acknowledges partial support from the Alfred P. Sloan Foundation through the Sloan Research Fellowship. MS acknowledges the support by the RIKEN Pioneering Project Evolution of Matter in the Universe (r-EMU) and Rikkyo University Special Fund for Research (Rikkyo SFR). NW and TP acknowledge the financial support of the GAČR EXPRO grant No. 21-13491X. Part of this work was performed under the auspices of the U.S. Department of Energy by Lawrence Livermore National Laboratory under Contract DE-AC52-07NA27344. The material is based upon work supported by NASA under award number 80GSFC21M0002. This work was supported by the JSPS Core-to-Core Program, JPJSCCA20220002. The material is based on work supported by the Strategic Research Center of Saitama University.

**Author Contributions** As the leader of the Centaurus cluster target team in the XRISM Science Team (XST), Y. Fujita led this research project and wrote the manuscript. K. Sato is the sub-leader of the target team, led the data analysis, and prepared the manuscript. He also contributed to the Resolve hardware development, integration tests, launch campaign, in-orbit operation, and calibration. K. Fukushima, F. Mernier, K. Matsushita, A. Simionescu, M. Kondo and A. Majumder analysed the data. Y.F., K.S., K.F., F.M., K.M., A.S. and K. Nakazawa discussed the results. T. Hayashi, T. Okajima, K. Tamura, Y. Maeda, M. Lowenstein, T. Yaqoob, E. Miller, M. Markevitch, F. Porter, M. Leutenegger, C. Kilbourne, and R. Kelley contributed useful comments on data calibration and systematic errors, as well as on the content of the manuscript. M. Sun, K. Hosogi, N. Werner and T. Plšek provided additional data. R. Mushotzky, I. Zhuravleva, and E. Behar helped to improve the manuscript. The science goals of XRISM were discussed and developed over 7 years by the XST, all members of which are authors of this manuscript. All the instruments were prepared by the joint efforts of the team. The manuscript was subject to an internal collaboration-wide review process. All authors reviewed and approved the final version of the manuscript.

**Author Information** Reprints and permissions information is available at [www.nature.com/reprints](http://www.nature.com/reprints). The authors declare no competing financial interests. Correspondence and requests for materials should be addressed to Y.F. (y-fujita@tmu.ac.jp) and K.S. (ksksato@mail.saitama-u.ac.jp).

**Data and code availability** The observational data analysed during this study are available in the NASA HEASARC repository (<https://heasarc.gsfc.nasa.gov/docs/hitomi/archive/>). The atomic databases used in this study are also available online (AtomDB, <http://www.atomdb.org/>).



## XRISM Collaboration

XRISM Collaboration<sup>1</sup>, Marc Audard<sup>2</sup>, Hisamitsu Awaki<sup>3</sup>, Ralf Ballhausen<sup>4,5,6</sup>, Aya Bamba<sup>7</sup>, Ehud Behar<sup>8</sup>, Rozenn Boissay-Malaquin<sup>9,5,6</sup>, Laura Brenneman<sup>10</sup>, Gregory V. Brown<sup>11</sup>, Lia Corrales<sup>12</sup>, Elisa Costantini<sup>13</sup>, Renata Cumbsee<sup>5</sup>, Maria Diaz-Trigo<sup>14</sup>, Chris Done<sup>15</sup>, Tadayasu Dotani<sup>16</sup>, Ken Ebisawa<sup>16</sup>, Megan E. Eckart<sup>11</sup>, Dominique Eckert<sup>2</sup>, Teruaki Enoto<sup>17</sup>, Satoshi Eguchi<sup>18</sup>, Yuichiro Ezoe<sup>19</sup>, Adam Foster<sup>10</sup>, Ryuichi Fujimoto<sup>16</sup>, Yutaka Fujita<sup>19</sup>, Yasuhiko Fukazawa<sup>20</sup>, Kotaro Fukushima<sup>16</sup>, Akihiro Furuzawa<sup>21</sup>, Luigi Gallo<sup>22</sup>, Javier A. Garcia<sup>5,23</sup>, Liyi Gu<sup>13</sup>, Matteo Guainazzi<sup>24</sup>, Kouichi Hagino<sup>7</sup>, Kenji Hamaguchi<sup>9,5,6</sup>, Isamu Hatsukade<sup>25</sup>, Katsuhiko Hayashi<sup>16</sup>, Takayuki Hayashi<sup>9,5,6</sup>, Natalie Hell<sup>11</sup>, Edmund Hodges-Kluck<sup>5</sup>, Ann Hornschemeier<sup>5</sup>, Yuto Ichinohe<sup>26</sup>, Manabu Ishida<sup>16</sup>, Kumi Ishikawa<sup>19</sup>, Yoshitaka Ishisaki<sup>19</sup>, Jelle Kaastra<sup>13,27</sup>, Timothy Kallman<sup>5</sup>, Erin Kara<sup>28</sup>, Satoru Katsuda<sup>29</sup>, Yoshiaki Kanamaru<sup>16</sup>, Richard Kelley<sup>5</sup>, Caroline Kilbourne<sup>5</sup>, Shunji Kitamoto<sup>30</sup>, Shogo Kobayashi<sup>31</sup>, Takayoshi Kohmura<sup>32</sup>, Aya Kubota<sup>33</sup>, Maurice Leutenegger<sup>5</sup>, Michael Loewenstein<sup>4,5,6</sup>, Yoshitomo Maeda<sup>16</sup>, Maxim Markevitch<sup>5</sup>, Hironori Matsumoto<sup>34</sup>, Kyoko Matsushita<sup>31</sup>, Dan McCammon<sup>35</sup>, Brian McNamara<sup>36</sup>, François Mernier<sup>4,5,6</sup>, Eric D. Miller<sup>28</sup>, Jon M. Miller<sup>12</sup>, Ikuyuki Mitsuishi<sup>37</sup>, Misaki Mizumoto<sup>38</sup>, Tsunefumi Mizuno<sup>39</sup>, Koji Mori<sup>25</sup>, Koji Mukai<sup>9,5,6</sup>, Hiroshi Murakami<sup>40</sup>, Richard Mushotzky<sup>4</sup>, Hiroshi Nakajima<sup>41</sup>, Kazuhiro Nakazawa<sup>37</sup>, Jan-Uwe Ness<sup>42</sup>, Kumiko Nobukawa<sup>43</sup>, Masayoshi Nobukawa<sup>44</sup>, Hirofumi Noda<sup>45</sup>, Hirokazu Odaka<sup>34</sup>, Shoji Ogawa<sup>16</sup>, Anna Ogorzalek<sup>4,5,6</sup>, Takashi Okajima<sup>5</sup>, Naomi Ota<sup>46</sup>, Stephane Paltani<sup>2</sup>, Robert Petre<sup>5</sup>, Paul Plucinsky<sup>10</sup>, Frederick Scott Porter<sup>5</sup>, Katja Pottschmidt<sup>9,5,6</sup>, Kosuke Sato<sup>29</sup>, Toshiki Sato<sup>47</sup>, Makoto Sawada<sup>30</sup>, Hiromi Seta<sup>19</sup>, Megumi Shidatsu<sup>3</sup>, Aurora Simionescu<sup>13</sup>, Randall Smith<sup>10</sup>, Hiromasa Suzuki<sup>16</sup>, Andrew Szymkowiak<sup>48</sup>, Hiromitsu Takahashi<sup>20</sup>, Mai Takeo<sup>29</sup>, Toru Tamagawa<sup>26</sup>, Keisuke Tamura<sup>9,5,6</sup>, Takaaki Tanaka<sup>49</sup>, Atsushi Tanimoto<sup>50</sup>, Makoto Tashiro<sup>29,16</sup>, Yukikatsu Terada<sup>29,16</sup>, Yuichi Terashima<sup>3</sup>, Yohko Tsuboi<sup>51</sup>, Masahiro Tsujimoto<sup>16</sup>, Hiroshi Tsunemi<sup>34</sup>, Takeshi G. Tsuru<sup>17</sup>, Hiroyuki Uchida<sup>17</sup>, Nagomi Uchida<sup>16</sup>, Yuusuke Uchida<sup>32</sup>, Hideki Uchiyama<sup>52</sup>, Yoshihiro Ueda<sup>53</sup>, Shinichiro Uno<sup>54</sup>, Jacco Vink<sup>55</sup>, Shin Watanabe<sup>16</sup>, Brian J. Williams<sup>5</sup>, Satoshi Yamada<sup>56</sup>, Shinya Yamada<sup>30</sup>, Hiroya Yamaguchi<sup>16</sup>, Kazutaka Yamaoka<sup>37</sup>, Noriko Yamasaki<sup>16</sup>, Makoto Yamauchi<sup>25</sup>, Shigeo Yamauchi<sup>46</sup>, Tahir Yaqoob<sup>9,5,6</sup>, Tomokage Yoneyama<sup>51</sup>, Tessei Yoshida<sup>16</sup>, Mihoko Yukita<sup>57,5</sup>, Irina Zhuravleva<sup>58</sup>, Marie Kondo<sup>29</sup>, Norbert Werner<sup>59</sup>, Tomáš Plšek<sup>59</sup>, Ming Sun<sup>60</sup>, Kokoro Hosogi<sup>60</sup>, Anwesh Majumder<sup>61,13</sup>

<sup>1</sup>Corresponding Authors: Y. Fujita (y-fujita@tmu.ac.jp) and K. Sato (ksksato@mail.saitama-u.ac.jp), <sup>2</sup>Department of Astronomy, University of Geneva, Versoix CH-1290, Switzerland, <sup>3</sup>Department of Physics, Ehime University, Ehime 790-8577, Japan, <sup>4</sup>Department of Astronomy, University of Maryland, College Park, MD 20742, USA, <sup>5</sup>NASA / Goddard Space Flight Center, Greenbelt, MD 20771, USA, <sup>6</sup>Center for Research and Exploration in Space Science and Technology, NASA / GSFC (CRESS II), Greenbelt, MD 20771, USA, <sup>7</sup>Department of Physics, University of Tokyo, Tokyo 113-0033, Japan, <sup>8</sup>Department of Physics, Technion, Technion City, Haifa 3200003, Israel, <sup>9</sup>Center for Space Science and Technology, University of Maryland, Baltimore County (UMBC), Baltimore, MD 21250, USA, <sup>10</sup>Center for Astrophysics | Harvard-Smithsonian, MA 02138, USA, <sup>11</sup>Lawrence Livermore National Laboratory, CA 94550, USA, <sup>12</sup>Department of Astronomy, University of Michigan, MI 48109, USA, <sup>13</sup>SRON Netherlands Institute for Space Research, Leiden, The Netherlands, <sup>14</sup>ESO, Karl-Schwarzschild-Strasse 2, 85748, Garching bei München, Germany, <sup>15</sup>Centre for Extragalactic Astronomy, Department of Physics, University of Durham, South Road, Durham DH1 3LE, UK, <sup>16</sup>Institute of Space and Astronautical Science (ISAS), Japan Aerospace Exploration Agency (JAXA), Kanagawa 252-5210, Japan, <sup>17</sup>Department of Physics, Kyoto University, Kyoto 606-8502, Japan, <sup>18</sup>Department of Economics, Kumamoto Gakuen University, Kumamoto 862-8680, Japan, <sup>19</sup>Department of Physics, Tokyo Metropolitan University, Tokyo 192-0397, Japan, <sup>20</sup>Department of Physics, Hiroshima University, Hiroshima 739-8526, Japan, <sup>21</sup>Department of Physics, Fujita Health University, Aichi 470-1192, Japan, <sup>22</sup>Department of Astronomy and Physics, Saint Mary's University, Nova Scotia B3H 3C3, Canada, <sup>23</sup>Cahill Center for Astronomy and Astrophysics, California Institute of Technology, Pasadena, CA 91125, USA, <sup>24</sup>European Space Agency (ESA), European Space Research and Technology Centre (ESTEC), 2200 AG, Noordwijk, The Netherlands, <sup>25</sup>Faculty of Engineering, University of Miyazaki, Miyazaki 889-2192, Japan, <sup>26</sup>RIKEN Nishina Center, Saitama 351-0198, Japan, <sup>27</sup>Leiden Observatory, University of Leiden, P.O. Box 9513, NL-2300 RA, Leiden, The Netherlands, <sup>28</sup>Kavli Institute for Astrophysics and Space Research, Massachusetts Institute of Technology, MA 02139, USA, <sup>29</sup>Department of Physics, Saitama University, Saitama 338-8570, Japan, <sup>30</sup>Department of Physics, Rikkyo University, Tokyo 171-8501, Japan, <sup>31</sup>Faculty of Physics, Tokyo University of Science, Tokyo 162-8601, Japan, <sup>32</sup>Faculty of Science and Technology, Tokyo University of Science, Chiba 278-8510, Japan, <sup>33</sup>Department of Electronic Information Systems, Shibaura Institute of Technology, Saitama 337-8570, Japan, <sup>34</sup>Department of Earth and Space Science, Osaka University, Osaka 560-0043, Japan, <sup>35</sup>Department of Physics, University of Wisconsin, WI 53706, USA, <sup>36</sup>Department of Physics and Astronomy, University of Waterloo, Ontario N2L 3G1, Canada, <sup>37</sup>Department of Physics, Nagoya University, Aichi 464-8602, Japan, <sup>38</sup>Science Research Education Unit, University of Teacher Education Fukuoka, Fukuoka 811-4192, Japan, <sup>39</sup>Hiroshima Astrophysical Science Center, Hiroshima University, Hiroshima 739-8526, Japan, <sup>40</sup>Department of Data Science, Tohoku Gakuin University, Miyagi 984-8588, Japan, <sup>41</sup>College of Science and Engineering, Kanto Gakuin University, Kanagawa 236-8501, Japan, <sup>42</sup>European Space Agency (ESA), European Space Astronomy Centre (ESAC), E-28692 Madrid, Spain, <sup>43</sup>Department of Science, Faculty of Science and Engineering, KINDAI University, Osaka 577-8502, Japan, <sup>44</sup>Department of Teacher Training and School Education, Nara University of Education, Nara 630-8528, Japan, <sup>45</sup>Astronomical Institute, Tohoku University, Miyagi 980-8578, Japan, <sup>46</sup>Department of Physics, Nara Women's University, Nara 630-8506, Japan, <sup>47</sup>School of Science and Technology, Meiji University, Kanagawa, 214-8571, Japan, <sup>48</sup>Yale Center for Astronomy and Astrophysics, Yale University, CT 06520-8121, USA, <sup>49</sup>Department of Physics, Konan University, Hyogo 658-8501, Japan, <sup>50</sup>Graduate School of Science and Engineering, Kagoshima University, Kagoshima 890-8580, Japan, <sup>51</sup>Department of Physics, Chuo University, Tokyo 112-8551, Japan, <sup>52</sup>Faculty of Education, Shizuoka University, Shizuoka 422-8529, Japan, <sup>53</sup>Department of Astronomy, Kyoto University, Kyoto 606-8502, Japan, <sup>54</sup>Nihon Fukushi University, Shizuoka 422-8529, Japan, <sup>55</sup>Anton Pannekoek Institute, the University of Amsterdam, Postbus 942491090 GE Amsterdam, The Netherlands, <sup>56</sup>RIKEN Cluster for Pioneering Research, Saitama 351-0198, Japan, <sup>57</sup>Johns Hopkins University, MD 21218, USA, <sup>58</sup>Department of Astronomy and Astrophysics, University of Chicago, Chicago, IL 60637, USA, <sup>59</sup>Department of Theoretical Physics and Astrophysics, Faculty of Science, Masaryk University, Kotlářská 2, Brno, 601 37, Czech Republic <sup>60</sup>Department of Physics and Astronomy, University of Alabama in Huntsville, Huntsville, AL 35899, USA <sup>61</sup>Astronomical Institute 'Anton Pannekoek', University of Amsterdam, Science Park 904, 1098 XH Amsterdam, The Netherlands